

Topological Signatures of History-Dependent Invariants in the Lorenz System: Deterministic Probes of Lobe Dynamics

B. A. Toledo^{a)}

Departamento de Física, Facultad de Ciencias, Universidad de Chile, Santiago, Chile

(Dated: 13 January 2026)

Building upon the recent discovery of history-dependent dynamical invariants in the Lorenz system, this work presents a systematic classification of a complete family of such conserved quantities and demonstrates their utility as deterministic probes of topological transitions. Through analysis of all 24 permutations in the augmented phase space, we identify eighteen distinct invariants (K_1 – K_{18}) organized into three regularization classes, while six permutations yield null results due to Schwarz integrability constraints. Each class is characterized by a distinct regularization polynomial that vanishes on the corresponding nullcline of the Lorenz flow: $p_I = y - x$, $p_{II} = y + x(z - \rho)$, and $p_{III} = xy - \beta z$.

The central result concerns the dynamical signatures that distinguish regularization classes. Statistical analysis of $N = 4 \times 10^6$ trajectory samples reveals that Class III invariants, whose polynomial parts contain the bilinear product xy , function as geometric probes of lobe-switching events. In the chaotic regime ($\rho = 28$), Class III exhibits elevated kurtosis ($\kappa_{III} \approx 15.8$ versus $\kappa_I \approx 8.2$) with heavy tails extending beyond $\pm 5\sigma$, while both classes show pronounced negative skewness ($S_I \approx -1.66$, $S_{III} \approx -2.73$). This divergence is absent in the pre-chaotic regime ($\rho = 23$), where both classes yield statistically similar distributions ($\kappa \approx 28.2$), confirming that the signatures arise specifically from the interaction between polynomial structure and chaotic dynamics.

Remarkably, the differential response $\Delta S = Q_{III} - Q_I$ between Class III and Class I evolution functions provides advance warning of separatrix crossings, with a prediction horizon governed by a shifted power law $\Delta t = t_{\min} + CA^{-n}$. Parametric analysis across $\beta \in [2.0, 3.2]$ reveals a robust linear relationship $n = m\beta + b$ with slope $m = 0.196 \pm 0.02$ ($R^2 = 0.94$), establishing that the predictive exponent scales with the stable eigenvalue. At the standard value $\beta = 8/3$, the fitted exponent $n \approx 1.0$ reflects the characteristic relaxation timescale along the stable manifold. This connection between algebraic classification and predictive capability demonstrates that Class III invariants encode the symbolic dynamics of the attractor's template structure. High-precision numerical validation using 80-digit arithmetic confirms conservation of all identified quantities to $O(10^{-36})$.

I. INTRODUCTION

The recent demonstration that the Lorenz system possesses history-dependent dynamical invariants has expanded the understanding of conservation laws in dissipative chaotic systems¹. That work established the existence of a non-local conserved quantity whose constancy along trajectories emerges through accumulation of the system's past via integral terms involving an auxiliary variable. The construction revealed structural organization within an augmented phase space and provided a characterization of unstable periodic orbits as level sets of this conserved functional.

The physical significance of these invariants extends beyond mathematical curiosity. In the Mori-Zwanzig formalism^{2,3}, memory effects arise naturally when projecting high-dimensional dynamics onto a reduced set of observables. The auxiliary variable $u(t)$ in this construction plays an analogous role: it accumulates the system's history in a manner that compensates for the apparent dissipation in the original three-dimensional flow. The regularization polynomials $p(x, y, z)$ that characterize each

class are not arbitrary mathematical artifacts; they are precisely the nullcline conditions of the Lorenz equations, suggesting that the invariant structure is intimately connected to the geometric skeleton of the flow.

The constructive method admits multiple distinct choices in the orthogonality ansatz used to augment the three-dimensional Lorenz phase space. The original work noted that “the constructive method employed can yield other conserved quantities,” deferring systematic exploration. This raises specific questions: How many independent history-dependent invariants exist? What governs their mathematical form? Do they possess distinct properties corresponding to different dynamical interpretations?

The present work addresses these questions through systematic analysis and reveals an unexpected connection between algebraic structure and dynamical sensitivity. By considering all 24 permutations of the phase space coordinates in the orthogonality construction, we identify exactly eighteen valid invariant structures and demonstrate that six permutations yield null results. The first coordinate in the permutation determines the regularization class, which in turn determines how the invariant responds to chaotic dynamics.

The central finding is that Class III invariants function as deterministic probes of topological transitions. The

^{a)}Electronic mail: btoledoc@uchile.cl

polynomial parts P_{III} contain terms involving the bilinear product xy , which changes sign at every lobe-switching event where the trajectory crosses the separatrix $x = 0$. Statistical analysis reveals that Class III evolution functions exhibit large-amplitude spikes synchronized with these crossings, while Class I evolution functions vary more smoothly. This differential response enables construction of a topological precursor signal that provides advance warning of separatrix crossings, with predictive capability governed by a power law whose exponent scales linearly with the stable eigenvalue β .

Independently, Hojman⁵ demonstrated that conservation laws can be constructed without recourse to Lagrangian or Hamiltonian formulations, establishing that the connection between symmetries and conserved quantities extends beyond the variational framework. The present construction shares this non-Noetherian character: the invariants K_n do not arise from continuous symmetries of an action functional but emerge from algebraic compatibility between the Lorenz flow and the orthogonality ansatz.

This paper is organized as follows. Section II reviews the constructive orthogonality method and introduces the permutation-based systematic exploration. Section III presents the complete family of eighteen invariants organized by permutation class, including regularization and the proof that permutations beginning with the auxiliary variable yield null results. Section IV establishes the functional independence structure and clarifies the role of invariant-specific auxiliary variables. Section V develops the geometric interpretation of history-dependent constraints. Section VI analyzes transformation properties under the discrete \mathbb{Z}_2 symmetry. Section VII provides numerical verification, statistical characterization, and the analysis of topological precursor detection. Section VIII synthesizes the results, including analysis of the physical interpretation of the invariants and their operational meaning.

II. SYSTEMATIC EXTENSION OF THE CONSTRUCTIVE METHOD

A. Review of the Orthogonality Approach

The Lorenz system is defined by the three coupled nonlinear ordinary differential equations

$$\dot{x} = \sigma(y - x), \quad (1)$$

$$\dot{y} = x(\rho - z) - y, \quad (2)$$

$$\dot{z} = xy - \beta z, \quad (3)$$

where σ , ρ , and β are positive parameters. For the classical parameter values $\sigma = 10$, $\rho = 28$, and $\beta = 8/3$, the system exhibits chaotic dynamics on the Lorenz attractor^{7,8}.

To construct conserved quantities for this odd-dimensional system, the phase space is augmented with

an auxiliary variable u , yielding a four-dimensional state space (x, y, z, u) . A candidate conserved quantity $C(x, y, z, u)$ must satisfy

$$\frac{dC}{dt} = \nabla C \cdot \mathbf{f} = 0, \quad (4)$$

where $\nabla \equiv (\partial_x, \partial_y, \partial_z, \partial_u)$, the flow vector is $\mathbf{f} \equiv (\dot{x}, \dot{y}, \dot{z}, \dot{u})$, and $\dot{u} = f(x, y, z)$ is to be determined self-consistently.

B. Connection to the Mori-Zwanzig Formalism

The introduction of the auxiliary variable $u(t)$ admits a natural interpretation within the framework of non-equilibrium statistical mechanics. The Mori-Zwanzig projection operator formalism^{2,3} establishes that when a high-dimensional system is projected onto a lower-dimensional subspace, the resulting equations necessarily acquire memory terms:

$$\frac{dA}{dt} = \Omega A + \int_0^t K(t-s)A(s) ds + F(t), \quad (5)$$

where $K(t)$ is a memory kernel encoding the influence of eliminated degrees of freedom and $F(t)$ represents a fluctuating force orthogonal to the resolved variables.

The Lorenz system, derived from a low-order truncation of the Navier-Stokes equations, represents such a projection. The regularized auxiliary variable $v_n(t)$, which evolves according to

$$v_n(t) = v_n(0) + \int_0^t Q_n(x(s), y(s), z(s)) ds, \quad (6)$$

can be understood as a deterministic resolution of the memory kernel: it explicitly tracks the accumulated effect of the trajectory's history that would otherwise manifest as non-Markovian dynamics.

A distinction must be drawn between two different approaches to treating unresolved degrees of freedom. In the Optimal Prediction framework of Chorin and collaborators², the fluctuating force $F(t)$ is treated stochastically: its effects are averaged over an ensemble, yielding a coarse-grained, probabilistic description. In contrast, the present construction constitutes a *deterministic embedding*: by extending the phase space with $v_n(t)$, we effectively absorb the orthogonal fluctuations into a resolved variable, achieving an exact closure in which $F(t) \equiv 0$ along any trajectory.

The paradigm for embedding dissipative systems within larger conservative frameworks has been developed systematically by Morrison⁴, who demonstrated that many dissipative systems admit Hamiltonian formulations in extended phase spaces. The present construction represents a concrete realization of this principle for the Lorenz system.

Physical scaling. In the original Rayleigh-Bénard convection context from which the Lorenz equations derive⁷, the state variables represent amplitudes of truncated Fourier modes: x corresponds to the convective velocity mode, while y and z correspond to temperature perturbation modes. The parameters σ , ρ , and β are dimensionless after appropriate scaling by the thermal diffusivity, cell height, and critical Rayleigh number. In this dimensionless formulation, the regularized auxiliary variable $v_n(t)$ inherits a kinematic interpretation as a generalized potential that accumulates historical effects of the modal amplitudes. For each regularization class, the polynomial factor $p_n(x, y, z)$ combines the physical modes in a specific manner: $p_I = y - x$ couples velocity and temperature perturbations, $p_{II} = y + x(z - \rho)$ involves the departure from criticality, and $p_{III} = xy - \beta z$ couples to the nonlinear heat flux term.

C. Permutation-Based Polynomial Construction

The key insight is that conserved quantities can be constructed systematically using permutations of the flow components as *heuristic generators* of polynomial candidates. We adopt a compact notation for permutations where we identify

$$1 \leftrightarrow x, \quad 2 \leftrightarrow y, \quad 3 \leftrightarrow z, \quad 4 \leftrightarrow u, \quad (7)$$

and write permutations as four-digit strings. For example, the permutation 1234 corresponds to the identity ordering (x, y, z, u) , while 2134 corresponds to (y, x, z, u) .

The inverse construction method. Rather than assuming that the gradient of a conserved quantity equals a permutation of the flow, we employ the permutation as a generator to synthesize a polynomial candidate. Given a permutation π , we construct a candidate scalar C by summing partial primitives:

$$C(x, y, z, u) = \sum_{i=1}^4 \int \pi(\mathbf{f})_i dq_i, \quad (8)$$

where $\pi(\mathbf{f})_i$ denotes the i -th component of the permuted flow vector and $\mathbf{q} = (x, y, z, u)$.

The resulting candidate $C(x, y, z, u)$ generically takes the form

$$C = P(x, y, z) + p(x, y, z) \cdot u, \quad (9)$$

where P is a polynomial and p is a polynomial factor coupling the auxiliary variable to the physical coordinates.

Classification by singularity structure. The polynomial $p(x, y, z)$ appearing in the denominator of the auxiliary evolution determines the singularity structure. Remarkably, the 18 valid permutations partition into exactly three families based on this polynomial:

- Permutations 1abc yield $p = y - x$ (Class I)
- Permutations 2abc yield $p = y + x(z - \rho)$ (Class II)

- Permutations 3abc yield $p = xy - \beta z$ (Class III)

This classification by regularization polynomial is the fundamental organizing principle.

III. COMPLETE FAMILY OF INVARIANTS

A. Organization by Permutation Class

The systematic exploration reveals an organizing principle: the first index in the permutation determines the regularization class. This leads to a natural partition:

- **Class I** (K_1 – K_6): Permutations 1abc (first coordinate is x)
- **Class II** (K_7 – K_{12}): Permutations 2abc (first coordinate is y)
- **Class III** (K_{13} – K_{18}): Permutations 3abc (first coordinate is z)
- **Null Class**: Permutations 4abc (first coordinate is u)

The null class consists of permutations where the auxiliary variable u occupies the first position. These permutations cannot yield valid invariants because the resulting consistency equations admit only trivial solutions.

B. Regularization Polynomials and Invariant-Specific Auxiliary Variables

Each class is characterized by a distinct regularization polynomial $p(x, y, z)$ that eliminates singularities. Each invariant K_n requires its own auxiliary variable $u_n(t)$ and regularized variable $v_n(t)$.

$$\begin{aligned} \text{Class I: } \quad p_I(x, y, z) &= y - x, \\ v_n^I &= \sigma(y - x)u_n, \quad n \in \{1, \dots, 6\}. \end{aligned} \quad (10)$$

$$\begin{aligned} \text{Class II: } \quad p_{II}(x, y, z) &= y + x(z - \rho), \\ v_n^{II} &= [y + x(z - \rho)]u_n, \quad n \in \{7, \dots, 12\}. \end{aligned} \quad (11)$$

$$\begin{aligned} \text{Class III: } \quad p_{III}(x, y, z) &= xy - \beta z, \\ v_n^{III} &= (\beta z - xy)u_n, \quad n \in \{13, \dots, 18\}. \end{aligned} \quad (12)$$

These polynomials possess clear physical interpretations within the context of the Lorenz equations. The Class I polynomial $p_I = y - x$ vanishes on the manifold where convective velocity equals horizontal temperature difference. The Class II polynomial $p_{II} = y + x(z - \rho)$ is precisely the right-hand side of Eq. (2) with opposite sign, vanishing at the y -nullcline where $\dot{y} = 0$. The Class III polynomial $p_{III} = xy - \beta z$ is the right-hand side of Eq. (3),

vanishing at the z -nullcline where $\dot{z} = 0$. This connection to the nullcline structure of the Lorenz flow establishes that the regularization classes encode geometric features of the dynamics.

It is interesting to note that the multiplicative structure $p(x, y, z) \cdot u_n$ implies a ‘‘gating’’ mechanism: when the polynomial $p(x, y, z)$ vanishes on nullclines, the memory’s contribution to the invariant is momentarily suppressed, regardless of the accumulated history encoded in u_n . This gating mechanism may explain the topological robustness observed in the statistical analysis, as the memory coupling is automatically reduced precisely where the flow undergoes critical transitions.

C. Structural Origin of the Regularized Evolution Equation

A key technical point: the evolution equation for the *regularized* variable v_n emerges as a function of (x, y, z) alone, independent of v_n itself. Consider an invariant of the form $K_n = P_n(x, y, z) + p(x, y, z) \cdot u_n$. The conservation requirement $dK_n/dt = 0$ yields:

$$\frac{dP_n}{dt} + \frac{dp}{dt}u_n + p\dot{u}_n = 0. \quad (13)$$

Defining $v_n = p \cdot u_n$ and differentiating:

$$\dot{v}_n = \dot{p} \cdot u_n + p \cdot \dot{u}_n = -\dot{P}_n. \quad (14)$$

The u_n -dependent terms cancel exactly, yielding $\dot{v}_n = Q_n(x, y, z) \equiv -\dot{P}_n$, which depends only on the physical coordinates.

D. Class I Invariants: Permutations 1abc

The six Class I invariants have form $K_n = P_n(x, y, z) + v_n^I$ where $v_n^I = \sigma(y - x)u_n$:

$$K_1(1234) = xy - \frac{xy^2}{2} + \frac{x^2z}{2} + yz\beta - \frac{x^2\rho}{2} + v_1^I, \quad (15)$$

$$K_2(1243) = -\frac{x^2y}{2} + \frac{y^2}{2} + xyz + xz\beta - xy\rho + v_2^I, \quad (16)$$

$$K_3(1324) = -\frac{xy^2}{2} + yz + \frac{xz^2}{2} + yz\beta - xz\rho + v_3^I, \quad (17)$$

$$K_4(1342) = -\frac{x^2y}{2} + yz + \frac{xz^2}{2} + xz\beta - xz\rho + v_4^I, \quad (18)$$

$$K_5(1423) = \frac{y^2}{2} + \frac{z^2\beta}{2} - xy\rho + v_5^I, \quad (19)$$

$$K_6(1432) = xy + \frac{x^2z}{2} - xyz + \frac{z^2\beta}{2} - \frac{x^2\rho}{2} + v_6^I. \quad (20)$$

E. Class II Invariants: Permutations 2abc

The six Class II invariants have form $K_n = P_n(x, y, z) + v_n^{II}$ where $v_n^{II} = [y + x(z - \rho)]u_n$:

$$K_7(2134) = -\frac{xy^2}{2} + yz\beta + \frac{x^2\sigma}{2} - xy\sigma + v_7^{II}, \quad (21)$$

$$K_8(2143) = -\frac{x^2y}{2} + xz\beta + xy\sigma - \frac{y^2\sigma}{2} + v_8^{II}, \quad (22)$$

$$K_9(2314) = -\frac{xy^2}{2} + yz\beta + xz\sigma - yz\sigma + v_9^{II}, \quad (23)$$

$$K_{10}(2341) = -\frac{x^2y}{2} + xz\beta + xz\sigma - yz\sigma + v_{10}^{II}, \quad (24)$$

$$K_{11}(2413) = -xyz + \frac{z^2\beta}{2} + xy\sigma - \frac{y^2\sigma}{2} + v_{11}^{II}, \quad (25)$$

$$K_{12}(2431) = -xyz + \frac{z^2\beta}{2} + \frac{x^2\sigma}{2} - xy\sigma + v_{12}^{II}. \quad (26)$$

F. Class III Invariants: Permutations 3abc

The six Class III invariants have form $K_n = P_n(x, y, z) + v_n^{III}$ where $v_n^{III} = (\beta z - xy)u_n$:

$$K_{13}(3124) = \frac{y^2}{2} + xyz - xy\rho + \frac{x^2\sigma}{2} - xy\sigma + v_{13}^{III}, \quad (27)$$

$$K_{14}(3142) = xy + \frac{x^2z}{2} - \frac{x^2\rho}{2} + xy\sigma - \frac{y^2\sigma}{2} + v_{14}^{III}, \quad (28)$$

$$K_{15}(3214) = \frac{y^2}{2} + xyz - xy\rho + xz\sigma - yz\sigma + v_{15}^{III}, \quad (29)$$

$$K_{16}(3241) = xy + \frac{x^2z}{2} - \frac{x^2\rho}{2} + xz\sigma - yz\sigma + v_{16}^{III}, \quad (30)$$

$$K_{17}(3412) = yz + \frac{xz^2}{2} - xz\rho + xy\sigma - \frac{y^2\sigma}{2} + v_{17}^{III}, \quad (31)$$

$$K_{18}(3421) = yz + \frac{xz^2}{2} - xz\rho + \frac{x^2\sigma}{2} - xy\sigma + v_{18}^{III}. \quad (32)$$

G. Null Class: Permutations 4abc

The six permutations beginning with 4 yield no valid invariants. Consider permutation 4123, corresponding to (u, x, y, z) . The orthogonality ansatz assigns

$$\nabla C = (\dot{u}, \dot{x}, \dot{y}, \dot{z}), \quad (33)$$

yielding:

$$\partial_x C = \dot{u} = f(x, y, z, u), \quad (34)$$

$$\partial_y C = \dot{x} = \sigma(y - x), \quad (35)$$

$$\partial_z C = \dot{y} = x(\rho - z) - y, \quad (36)$$

$$\partial_u C = \dot{z} = xy - \beta z. \quad (37)$$

TABLE I. Master table of permutations: correspondence between invariant index K_n and generating permutation π . Indices 1–4 map to coordinates x, y, z, u respectively.

Class I		Class II		Class III	
K_n	π	K_n	π	K_n	π
K_1	1234	K_7	2134	K_{13}	3124
K_2	1243	K_8	2143	K_{14}	3142
K_3	1324	K_9	2314	K_{15}	3214
K_4	1342	K_{10}	2341	K_{16}	3241
K_5	1423	K_{11}	2413	K_{17}	3412
K_6	1432	K_{12}	2431	K_{18}	3421

Null Class: Permutations 4123, 4132, 4213, 4231, 4312, 4321 yield no valid invariants due to Schwarz integrability constraints.

Schwarz’s theorem for mixed partial derivatives requires $\partial_{yu}C = \partial_{uy}C$. From Eqs. (35) and (37):

$$\partial_u(\partial_y C) = \partial_u[\sigma(y-x)] = 0, \quad (38)$$

$$\partial_y(\partial_u C) = \partial_y[xy - \beta z] = x. \quad (39)$$

Equality requires $0 = x$, a constraint that restricts C to the hyperplane $x = 0$, which is not invariant under the Lorenz flow. No smooth invariant satisfying ansatz (33) exists throughout phase space.

The impossibility of null-class invariants admits a physical interpretation in terms of causal hierarchy. In the valid classes (I–III), the auxiliary variable u is *driven* by the physical coordinates through an evolution equation $\dot{u} = f(x, y, z)$ determined by the consistency conditions. The null class attempts the reverse: placing u first in the permutation ordering would require the physical flow to be determined by the auxiliary dynamics. This violates the fundamental asymmetry between the “system” (physical coordinates) and the “memory” (auxiliary variable). In the language of Mori-Zwanzig theory, the memory kernel must depend on the resolved variables, not vice versa.

The complete classification is summarized in Table I.

IV. FUNCTIONAL INDEPENDENCE AND AUXILIARY VARIABLE STRUCTURE

A. Boundedness of Regularized Variables

A consequence of the conservation laws is that regularized variables $v_n(t)$ remain bounded for all time. From conservation $K_n = P_n(x, y, z) + v_n = c_n$:

$$v_n(t) = c_n - P_n(x(t), y(t), z(t)). \quad (40)$$

Since P_n is polynomial and the Lorenz attractor is compact, $v_n(t)$ is bounded.

Zero time-average. Boundedness implies that $Q_n = \dot{v}_n$ has zero time-average with respect to the ergodic measure:

$$\langle Q_n \rangle_{\text{SRB}} = \lim_{T \rightarrow \infty} \frac{1}{T} \int_0^T Q_n(x(t), y(t), z(t)) dt = 0. \quad (41)$$

B. Constraints on Trajectory Histories

For any selection of three invariants $\{K_I, K_{II}, K_{III}\}$ with one from each regularization class, the corresponding constraints

$$K_I = P_I(x, y, z) + v_I = c_1, \quad (42)$$

$$K_{II} = P_{II}(x, y, z) + v_{II} = c_2, \quad (43)$$

$$K_{III} = P_{III}(x, y, z) + v_{III} = c_3, \quad (44)$$

are functionally independent and, together with the initial state (x_0, y_0, z_0) , characterize a trajectory up to the discrete \mathbb{Z}_2 symmetry.

At $t = 0$, with $v_n(0) = 0$, the invariant values are determined by

$$c_n = P_n(x_0, y_0, z_0). \quad (45)$$

Since P_I, P_{II} , and P_{III} are algebraically distinct polynomials, the map $(x_0, y_0, z_0) \mapsto (c_1, c_2, c_3)$ has full rank at generic points.

C. The Triad Construction

Selecting one invariant from each regularization class,

$$\mathcal{T} = \{K_I, K_{II}, K_{III}\}, \quad (46)$$

provides a canonical set of three independent history constraints. Each Triad defines a “fingerprint” (c_1, c_2, c_3) that can be computed instantaneously from (x_0, y_0, z_0) via Eq. (45). The canonical Triad $\{K_5, K_{11}, K_{13}\}$ consists of even invariants under \mathbb{Z}_2 , so the fingerprint identifies trajectories up to discrete symmetry.

V. GEOMETRIC INTERPRETATION

A. Invariants as Constraints on Trajectory Histories

The history-dependent invariants differ qualitatively from classical conservation laws. In Hamiltonian mechanics, $H(q, p) = E$ defines a hypersurface in instantaneous phase space; trajectories are confined to this surface for all time. The constraint is local in time.

The invariants $K_n = P_n(x, y, z) + v_n = c_n$ define constraints of a different character. The regularized variable $v_n(t)$ emerges as a *functional of the trajectory history*:

$$v_n[\gamma] = \int_\gamma Q_n(x, y, z) dt, \quad (47)$$

where γ denotes the trajectory from $t = 0$ to the current time. The constraint $K_n = c_n$ couples the instantaneous state (x, y, z) to the accumulated history v_n ; it is non-local in time.

It is worth noting that invariants from different regularization classes “observe” the trajectory through fundamentally different lenses: Class I responds to the $y-x$ nullcline structure, while Class III responds to the z -nullcline and its connection to lobe-switching events. This geometric distinction drives the statistical divergence observed in the chaotic regime.

B. Visualization of Constraint Surfaces

Figure 1 displays constraint surfaces for the canonical Triad $\mathcal{T} = \{K_5, K_{11}, K_{13}\}$ anchored to an unstable periodic orbit (UPO). The three-dimensional visualization (panel a) depicts the level surfaces of the invariant polynomials in the Lorenz phase space: $P_5(x, y, z) = c_1$ (Class I, blue), $P_{11}(x, y, z) = c_2$ (Class II, green), and $P_{13}(x, y, z) = c_3$ (Class III, red), where the constants c_n are determined by the UPO geometry. A representative chaotic trajectory illustrates the system’s evolution relative to these intersecting conserved manifolds.

Panel (b) presents a two-dimensional cross-section on an optimized Poincaré plane. The local coordinates (η, ξ) are defined by $\mathbf{P}(\eta, \xi) = \mathbf{P}_0 + \eta \hat{\mathbf{u}} + \xi \hat{\mathbf{w}}$, where \mathbf{P}_0 is a point on the unstable periodic orbit and $\{\hat{\mathbf{u}}, \hat{\mathbf{w}}\}$ form an orthonormal basis of a plane whose orientation was numerically optimized to maximize the angular separation between the three level curves. The curves meet at a single point (the UPO crossing), confirming that all three constraints are simultaneously satisfied.

VI. SYMMETRY ANALYSIS

A. The Discrete \mathbb{Z}_2 Symmetry

The Lorenz system possesses the discrete symmetry

$$\mathcal{S} : (x, y, z) \rightarrow (-x, -y, z), \quad (48)$$

which leaves Eqs. (1)–(3) invariant.

The regularization polynomials transform under \mathcal{S} as follows:

$$p_I = y - x \rightarrow -p_I \quad (\text{odd}), \quad (49)$$

$$p_{II} = y + x(z - \rho) \rightarrow -p_{II} \quad (\text{odd}), \quad (50)$$

$$p_{III} = xy - \beta z \rightarrow p_{III} \quad (\text{even}). \quad (51)$$

Table II presents the complete parity classification. Six invariants ($K_5, K_6, K_{11}, K_{12}, K_{13}, K_{14}$) are purely even; four (K_3, K_4, K_9, K_{10}) are purely odd; eight possess mixed parity.

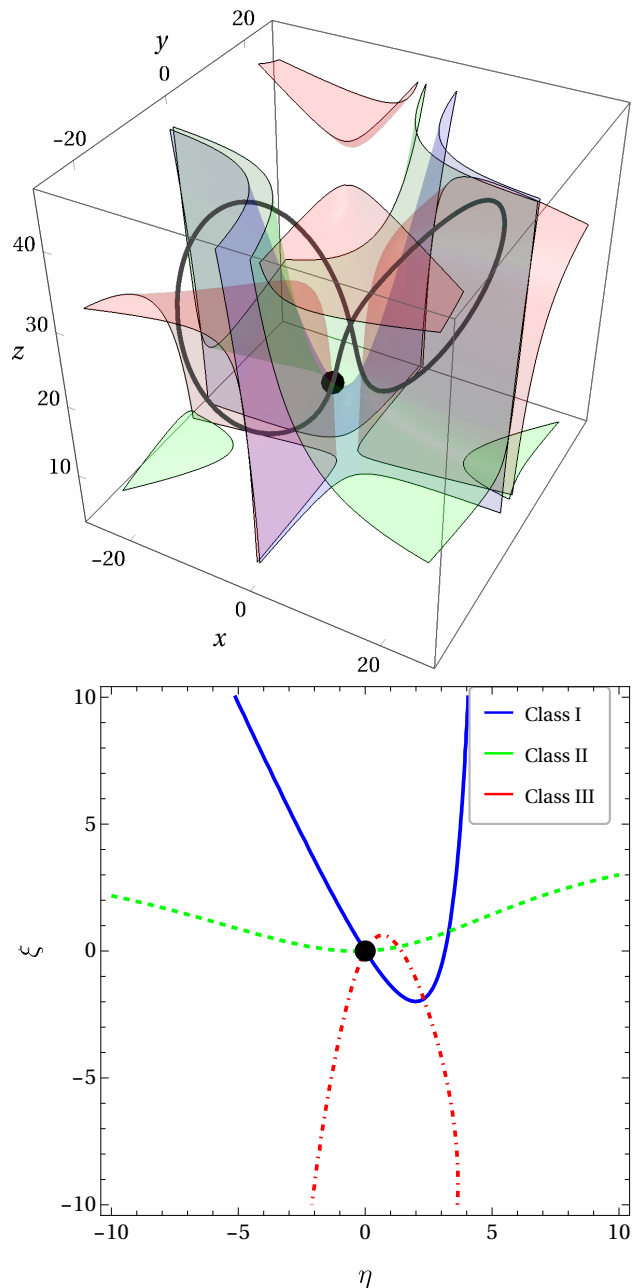


FIG. 1. **Geometric structure of the regularization classes.** (a) Three-dimensional representation of the level surfaces of the invariant polynomials in the Lorenz phase space: $P_5 = c_1$ (Class I, blue solid), $P_{11} = c_2$ (Class II, green dashed), and $P_{13} = c_3$ (Class III, red dot-dashed), where the constants are anchored to an unstable periodic orbit. A representative chaotic trajectory (dark curve) illustrates the system’s evolution relative to these conserved manifolds. The black dot marks a point on the UPO. (b) Two-dimensional cross-section in local coordinates (η, ξ) on an optimized Poincaré plane showing the topological relationship between the three regularization classes: $K_5 = c_1$ (Class I, blue solid), $K_{11} = c_2$ (Class II, green dashed), and $K_{13} = c_3$ (Class III, red dot-dashed). The intersection point corresponds to configurations where all three polynomial constraints are satisfied simultaneously on the UPO. Parameters: $\sigma = 10$, $\rho = 28$, $\beta = 8/3$.

TABLE II. Classification of invariants by \mathbb{Z}_2 parity of P_n . E = even; O = odd; M = mixed.

Class	Invariants	Parity	Odd terms
I	K_5, K_6	E	–
	K_3, K_4	O	yz, xz
	$K_1(yz), K_2(xz)$	M	–
II	K_{11}, K_{12}	E	–
	K_9, K_{10}	O	yz, xz
	$K_7(yz), K_8(xz)$	M	–
III	K_{13}, K_{14}	E	–
	$K_{15}-K_{18}$	M	yz, xz

TABLE III. Conservation errors $|K(T) - K(0)|$ for Triad invariants after one UPO period ($T \approx 1.56$). Calculations performed with 80-digit working precision.

Invariant	Class	Error
K_5	I	3.45×10^{-36}
K_{11}	II	9.35×10^{-38}
K_{13}	III	3.68×10^{-38}

VII. NUMERICAL VERIFICATION AND STATISTICAL ANALYSIS

A. High-Precision Verification

We performed numerical integration using 80-digit extended precision arithmetic in Mathematica with the `StiffnessSwitching` method, which automatically adapts to handle stiff intervals during separatrix crossings. Initial conditions and parameters were specified using exact arithmetic (integers and rationals) to prevent precision contamination.

For each invariant K_n , we verified:

1. *Conservation*: $|K_n(T) - K_n(0)| < 10^{-35}$ over $T = 5000$ time units.
2. *Boundedness*: $v_n(t)$ fluctuates within a finite range consistent with $v_n = c_n - P_n$.
3. *Zero mean*: $|\langle Q_n \rangle_T| \rightarrow 0$ as T^{-1} .

Table III presents conservation errors for the canonical Triad after one UPO period. Errors of order 10^{-36} – 10^{-38} confirm conservation to numerical precision. With 80-digit working precision, the machine epsilon is $\sim 10^{-80}$; the observed errors of $O(10^{-37})$ reflect normal accumulation of roundoff during integration, confirming that the conservation laws are satisfied to the limits of numerical precision.

B. Statistical Analysis of Auxiliary Evolution Functions

We examine whether invariants from different regularization classes exhibit distinct dynamical signatures. For each invariant $K_n = P_n(x, y, z) + v_n$, the evolution function

$$Q_n(x, y, z) \equiv \dot{v}_n = -\frac{dP_n}{dt} \quad (52)$$

represents the instantaneous rate at which v_n evolves to maintain conservation. Statistics were computed from $N = 4 \times 10^6$ trajectory samples (integration time $T = 400$ after transient removal, sampling interval $\Delta t = 10^{-4}$).

Pre-chaotic regime ($\rho = 23$). Both classes yield statistically similar distributions (Fig. 2a). Kurtosis values $\kappa_I \approx 28.1$ and $\kappa_{III} \approx 28.3$ are effectively identical. This baseline establishes that there is no intrinsic bias in the Class III formulation; the statistical equivalence confirms that both classes respond identically to the simple spiral dynamics without lobe-switching.

Chaotic regime ($\rho = 28$). A clear structural divergence emerges (Fig. 2b). The standardized distributions reveal different tail structures:

Differential intermittency. Class III exhibits substantially higher kurtosis ($\kappa_{III} \approx 15.8$) compared to Class I ($\kappa_I \approx 8.2$), a 93% increase. The heavy tails extending beyond $\pm 5\sigma$ indicate that Class III conservation is subject to sporadic large-amplitude events (“spikes”) punctuating quiescent intervals.

Asymmetry structure. Both classes display pronounced negative skewness in the chaotic regime, with Class III exhibiting even stronger asymmetry ($S_{III} \approx -2.73$) than Class I ($S_I \approx -1.66$). This indicates that extreme negative excursions dominate the fluctuation statistics for both classes, but the effect is amplified in Class III due to the rapid sign changes of the xy term during separatrix crossings. The enhanced negative skewness of Class III reflects the geometric asymmetry of lobe-switching events: trajectories accelerate sharply as they approach the separatrix from one direction.

Interpretation. The elevated kurtosis of Class III correlates with lobe-switching events. At separatrix crossings, P_{III} varies rapidly due to its xy -terms, forcing rapid adjustments in the Class III evolution function. Class I quantities lack this geometric sensitivity due to the smoothing effect of the z^2 term in $P_5 = y^2/2 + \beta z^2/2 - xy\rho$.

Pre-chaotic versus chaotic kurtosis. A noteworthy feature is that the pre-chaotic regime ($\rho = 23$) exhibits substantially higher kurtosis ($\kappa \approx 28.2$) than the chaotic regime ($\kappa_I \approx 8.2$). This counterintuitive result reflects a fundamental difference in statistical structure. At $\rho = 23$, the system operates near the subcritical Hopf bifurcation where trajectories exhibit complex transient dynamics: long intervals of quiescence near local attractors are punctuated by abrupt escapes. These rare but intense bursts generate distributions with pronounced heavy tails, yielding elevated kurtosis. In contrast, fully

TABLE IV. Statistical characterization of evolution functions $Q_n(t)$ for Class I (K_5) and Class III (K_{13}). Kurtosis κ measures tail weight (Gaussian: $\kappa = 3$); skewness S measures asymmetry. Statistics computed from $N = 4 \times 10^6$ samples over $T = 400$ time units.

Statistic	$\rho = 23$ (pre-chaotic)		$\rho = 28$ (chaotic)	
	Q_I	Q_{III}	Q_I	Q_{III}
Kurtosis κ	28.1	28.3	8.2	15.8
Skewness S	-0.16	-0.44	-1.66	-2.73

developed chaos at $\rho = 28$ produces more ergodic and mixing dynamics, with fluctuations distributed more uniformly across time.

C. Class III as a Topological Probe

The Class III evolution function $Q_{III}(t)$ functions as a *symbolic marker* that signals each addition to the trajectory’s symbolic sequence. In the standard symbolic dynamics description⁶, each visit to the left lobe is encoded as L , each visit to the right lobe as R . The sequence $\dots LLRLLRLR \dots$ captures the trajectory’s itinerary through the attractor.

The evolution function $Q_{III}(t)$ provides a continuous encoding of this discrete dynamics:

- *Quiescent intervals* ($|Q_{III}| \ll |Q_{III}|_{\max}$): The trajectory remains within a single lobe; no symbols are added.
- *Spike events* ($|Q_{III}| \sim |Q_{III}|_{\max}$): The trajectory crosses the separatrix; a new symbol is appended.

This establishes $Q_{III}(t)$ as a *geometric probe of topological transitions*: the integrated area under each spike corresponds to the “topological contribution” of that symbol transition. Class III invariants thereby encode the discrete symbolic structure of the chaotic flow, while Class I invariants probe the continuous dynamics.

D. Topological Precursor Detection

The differential response between Class III and Class I evolution functions provides the basis for a topological precursor detector. We construct the differential signal

$$\Delta S(t) = Q_{13}(t) - Q_5(t), \quad (53)$$

which isolates the topological sensitivity of Class III from the continuous dynamics tracked by Class I.

Detection protocol. Define an alert threshold \mathcal{A}_{th} based on the amplitude of $\Delta S(t)$. When $|\Delta S(t)|$ exceeds \mathcal{A}_{th} , a precursor event is registered. The latency Δt is defined as the time interval between the precursor signal and the subsequent separatrix crossing (zero-crossing of $x(t)$).

Scaling law. Figure 2(c) reveals a remarkable empirical relationship between the spike amplitude \mathcal{A} and the prediction latency Δt . The data are well-described by a shifted power law:

$$\Delta t = t_{\min} + C\mathcal{A}^{-n}, \quad (54)$$

with fitted parameters:

$$t_{\min} \approx 0.14, \quad (55)$$

$$n \approx 1.0. \quad (56)$$

Connection to the stable eigenvalue. Parametric analysis across the range $\beta \in [2.0, 3.2]$ reveals that the exponent n scales linearly with the stable eigenvalue: $n = m\beta + b$ with slope $m = 0.196 \pm 0.02$ and $b \approx 0.5$, with $R^2 = 0.94$. At the standard value $\beta = 8/3$, this yields $n \approx 1.0$. The linear relationship is physically significant: the Class III regularization polynomial $p_{III} = xy - \beta z$ explicitly contains β , and the predictive capability is governed by relaxation along the stable manifold (the z -direction near the fixed points). The proportionality constant $m \approx 0.2$ indicates that the differential sensor effectively integrates trajectory information over approximately five relaxation timescales ($\tau = 1/\beta$) before generating a detectable precursor signal.

The physical interpretation is as follows. As the trajectory approaches the separatrix, the product xy decreases toward zero while z relaxes toward the unstable manifold. The rate of approach is governed by the stable eigenvalue $-\beta$. Trajectories with larger initial departure from the separatrix (smaller \mathcal{A}) require longer relaxation times before crossing, yielding the inverse power-law relationship.

Intrinsic latency. The parameter $t_{\min} \approx 0.14$ represents the minimum prediction horizon, determined by the phase-space separation between the unstable manifold and the Poincaré section $x = 0$. Even for the strongest precursor signals, the trajectory requires a finite time to traverse this geometric gap.

Bimodal structure. The scatter plot in Fig. 2(c) reveals a secondary “phantom branch” at low amplitudes and long latencies (inset). These events correspond to trajectories entering the alert zone far from the actual separatrix crossing, subsequently executing partial orbits before the true transition. The bimodal distribution directly manifests the heavy-tailed statistics documented in Table IV.

VIII. DISCUSSION

A. Principal Result: Class-Dependent Dynamical Sensitivity

The central result of this work is that different regularization classes probe different aspects of chaotic dynamics. This distinction transcends formal mathematical structure and reveals operational differences in how the invariants respond to trajectory evolution.

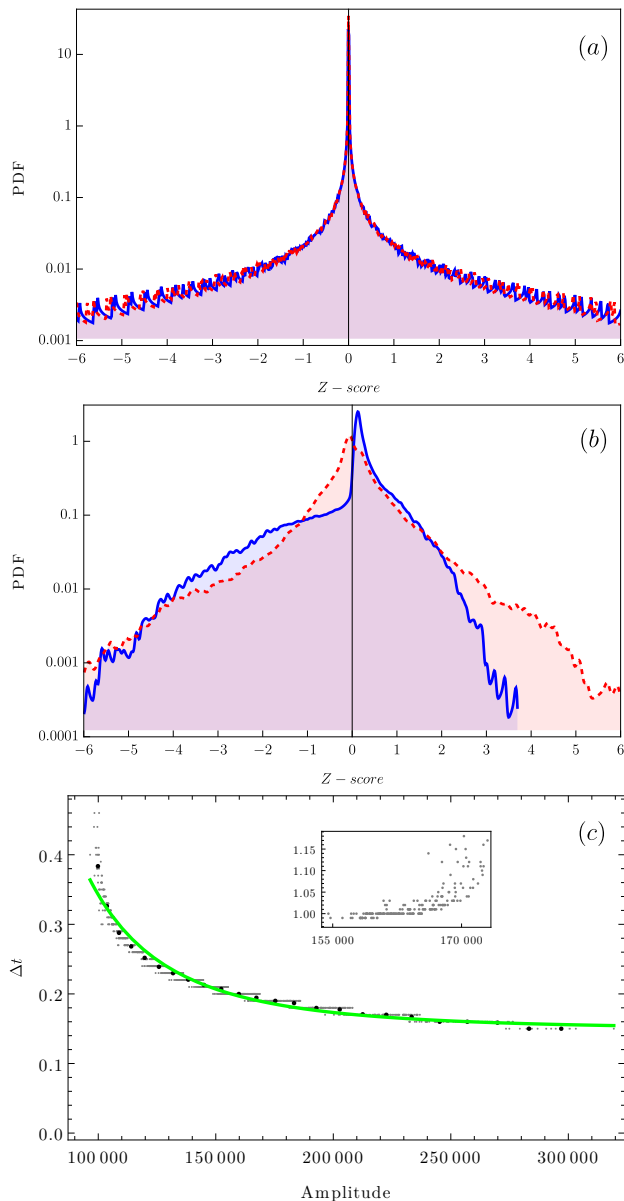


FIG. 2. Statistical signatures and topological precursor detection. Probability density functions of standardized evolution functions Q_I (Class I, solid blue) and Q_{III} (Class III, dashed red) on semi-logarithmic scale, with Z-score normalization. (a) Pre-chaotic regime ($\rho = 23$): distributions are statistically similar ($\kappa \approx 28.2$ for both), establishing that no intrinsic bias exists in the Class III formulation. (b) Chaotic regime ($\rho = 28$): Class III develops heavier tails ($\kappa_{III} \approx 15.8$ versus $\kappa_I \approx 8.2$) extending beyond $\pm 5\sigma$, indicating enhanced intermittency at topological transitions. Both classes exhibit pronounced negative skewness ($S_I \approx -1.66$, $S_{III} \approx -2.73$). (c) Scaling law for the topological precursor. Latency Δt (time from precursor signal to separatrix crossing) versus spike amplitude \mathcal{A} of the differential signal $\Delta S = Q_{13} - Q_5$. Gray points: individual events; black circles: logarithmically binned averages; green curve: fitted shifted power law $\Delta t = t_{\min} + C\mathcal{A}^{-n}$ with $t_{\min} \approx 0.14$ and $n \approx 1.0$ at $\beta = 8/3$. Parametric analysis reveals that n scales linearly with β (slope $m \approx 0.196$, $R^2 = 0.94$), establishing that predictive capability is governed by relaxation along the stable manifold. Statistics computed from $N = 4 \times 10^6$ trajectory samples.

Class I invariants as continuous probes. The polynomial parts P_I contain terms like z^2 that vary continuously throughout the attractor. The evolution function $Q_I = \dot{v}_I$ exhibits moderate intermittency ($\kappa_I \approx 8.2$), with variance distributed across quiescent and active intervals alike. These invariants track smooth, continuous aspects of the flow.

Class III invariants as topological probes. The polynomial parts P_{III} couple directly to the bilinear product xy , which changes sign at every lobe transition. The evolution function Q_{III} exhibits elevated kurtosis ($\kappa_{III} \approx 15.8$) with spikes synchronized to separatrix crossings and quiescent intervals between transitions. These invariants function as geometric markers of the symbolic dynamics, encoding the discrete topological structure of the attractor.

Differential detection. The complementarity between classes enables construction of a differential detector $\Delta S = Q_{III} - Q_I$ that acts as a “topological band-pass filter”: it cancels the continuous rotational dynamics to isolate the hyperbolic singularities associated with lobe-switching events.

B. Physical Interpretation of the Conservation Laws

The history-dependent invariants occupy a distinctive position in the taxonomy of conservation laws. They do not arise from a variational principle or symmetry of an action functional; rather, they emerge from the algebraic structure of the Lorenz flow when augmented with auxiliary variables. Conservation is enforced by construction: $\dot{v}_n = -\dot{P}_n$ by definition.

This non-Noetherian character connects to the broader framework established by Hojman⁵, who demonstrated that conservation laws can be constructed without Lagrangian or Hamiltonian formulations. The present invariants represent a concrete realization of this principle for a dissipative chaotic system.

Non-triviality. The existence of the null class demonstrates that conservation cannot be achieved for arbitrary polynomials. The failure of six permutations to yield valid invariants proves that the Lorenz structure genuinely constrains which polynomial forms are compatible with the orthogonality ansatz.

Main results. This construction yields two principal results:

1. The *classification* of compatible polynomial structures encodes information specific to the Lorenz dynamics. Eighteen valid invariants organized into three regularization classes reflect algebraic compatibility between the Lorenz flow and the orthogonality ansatz.
2. The *distinct dynamical signatures* exhibited by different classes provide complementary probes of attractor geometry. Class III invariants function as

geometric markers of topological transitions, while Class I invariants track continuous dynamics.

C. Connection to Template Theory

The connection between Class III sensitivity and lobe-switching events resonates with the template theory of chaotic attractors⁶. The Lorenz attractor possesses a branched manifold structure that captures the essential stretching and folding operations; periodic orbits can be classified by their knot type, determined by the sequence of lobe visits.

The evolution function $Q_{\text{III}}(t)$ is functionally equivalent to a continuous Poincaré section detector: each spike marks a crossing of the template’s branch line. The integrated area under each spike corresponds to the “topological contribution” of that symbol transition, providing a continuous encoding of the discrete symbolic dynamics.

The scaling law $\Delta t = t_{\text{min}} + CA^{-n}$ with $n \propto \beta$ establishes a quantitative link between the algebraic structure of the invariants and the eigenvalue structure of the flow. The stable eigenvalue β governs relaxation along the z -direction, and the Class III regularization polynomial $p_{\text{III}} = xy - \beta z$ explicitly couples to this mode. The linear relationship $n = m\beta + b$ with $m \approx 0.2$ indicates that the detector integrates information over multiple relaxation cycles.

D. Robustness and Practical Utility

The invariants provide several practical utilities:

1. *Numerical accuracy monitors*: Conservation violations signal integration errors.
2. *Periodic orbit fingerprints*: The Triad (c_1, c_2, c_3) provides intrinsic orbit labels.
3. *Trajectory classification*: Different initial conditions yield different fingerprints.
4. *Topological precursor detection*: The differential signal ΔS provides advance warning of separatrix crossings.

The structural redundancy of 18 invariants provides internal consistency checks. For pairs within the same class, $v_n - v_m = P_m - P_n$ must hold exactly. Comparing invariants from different classes enables filtering topology from noise: a spike in Q_{III} accompanied by smooth Q_{I} behavior confirms a genuine separatrix crossing, whereas uncorrelated fluctuations suggest stochastic perturbation.

E. Experimental Realization and Long-Time Stability

While the differential detector (Sec. VIID) is optimal for short-term prediction of imminent separatrix

crossings, practical implementation in physical experiments or long numerical simulations requires addressing two fundamental challenges that arise from the history-dependent nature of the invariants.

The secular drift problem. Since $v_n(t)$ integrates the trajectory history via $v_n = \int_0^t Q_n ds$, any small but persistent perturbation (thermal noise, roundoff error, measurement uncertainty) accumulates over time. In an open-loop implementation, this produces a secular drift: the invariant ceases to be constant and executes a random walk with variance growing as $\sigma^2 \sim t$, rendering long-term conservation unusable.

The unknown initial condition problem. Computing the conserved value $c_n = P_n(x_0, y_0, z_0)$ requires knowledge of the exact initial state. In chaotic experimental systems, information about the initial condition is lost exponentially fast. An observer who begins measurement at time $t > 0$ cannot determine the invariant value without access to the prior history.

Both problems are resolved by the *operational reset protocol*. Rather than treating v_n as an open-ended integral accumulating from $t = 0$ to the current time t , one selects a Poincaré section Σ transverse to the flow (for example, the plane $x = 0$ with $\dot{x} > 0$). Each time the trajectory crosses Σ , the accumulated variable is reset: $v_n \rightarrow 0$. The physically meaningful quantity becomes the discrete sequence of cycle-integrated values

$$\Delta v_n^{(k)} = \int_{t_k}^{t_{k+1}} Q_n(x(s), y(s), z(s)) ds, \quad (57)$$

where t_k denotes the k -th crossing of Σ .

This cyclic formulation transforms the open-loop integral (unbounded, drift-prone) into a closed-loop measurement (bounded, self-correcting). For unstable periodic orbits, the value $\Delta v_n^{(\text{UPO})}$ after one complete period is a fixed topological-dynamical invariant, providing an unambiguous orbit fingerprint independent of when measurement begins. The statistical distribution of $\{\Delta v_n^{(k)}\}$ across many cycles encodes intrinsic properties of the attractor’s ergodic structure, connecting the continuous dynamics to discrete symbolic analysis.

IX. CONCLUSION

This work has presented a systematic exploration of history-dependent dynamical invariants in the Lorenz system and demonstrated their utility as deterministic probes of topological transitions. The investigation began with a methodical question: given that the orthogonality construction admits multiple polynomial forms, how many independent invariants exist, and do they possess distinct dynamical signatures? The answer reveals an unexpectedly rich algebraic structure with direct physical consequences.

The permutation-based enumeration of the augmented phase space yields a complete classification. Of the 24

possible ansätze, exactly 18 produce valid invariants organized into three regularization classes, while the remaining 6 fail due to Schwarz integrability constraints. This partition is not arbitrary; the first coordinate in each permutation determines the regularization polynomial, which in turn controls the geometric coupling between the invariant and the Lorenz flow. The null class, where the auxiliary variable occupies the leading position, embodies a fundamental asymmetry: the memory kernel must depend on the resolved variables, not vice versa.

The central discovery concerns the operational distinction between regularization classes. Statistical analysis of $N = 4 \times 10^6$ trajectory samples demonstrates that Class III invariants, whose polynomial parts contain the bilinear product xy , function as geometric probes of lobe-switching events. In the chaotic regime, Class III exhibits elevated kurtosis ($\kappa_{\text{III}} \approx 15.8$ versus $\kappa_{\text{I}} \approx 8.2$) with heavy tails synchronized to separatrix crossings, while both classes remain statistically similar in the pre-chaotic regime. This divergence confirms that the signatures arise specifically from the interaction between polynomial structure and chaotic dynamics, rather than from any intrinsic bias in the formulation.

The complementarity between classes enables construction of a differential detector $\Delta S = Q_{13} - Q_5$ that provides advance warning of topological transitions. The prediction horizon follows a shifted power law $\Delta t = t_{\text{min}} + CA^{-n}$, where parametric analysis across $\beta \in [2.0, 3.2]$ reveals that the exponent scales linearly with the stable eigenvalue: $n = m\beta + b$ with $m = 0.196 \pm 0.02$ and $b \approx 0.5$, with $R^2 = 0.94$. This quantitative link between algebraic classification and predictive capability establishes that the Class III regularization polynomial $p_{\text{III}} = xy - \beta z$ explicitly couples to the relaxation mode governing separatrix approach.

High-precision numerical validation using 80-digit arithmetic confirms conservation to $O(10^{-36})$, demonstrating that the invariants are exact within the limits of numerical representation. For practical implementation in physical experiments or long numerical simulations, the operational reset protocol transforms the history-dependent integrals into cycle-bounded measurements anchored to a Poincaré section. This cyclic formulation eliminates secular drift and enables robust characterization even when initial conditions are unknown.

The framework established here opens several avenues for future investigation. Whether the linear scaling $n \propto \beta$ holds for other sensor pairs from different classes re-

mains to be tested. The complete structure of the 192-element family obtained by allowing independent component signs has not been explored. Most significantly, the question of whether analogous history-dependent invariants exist in other dissipative chaotic systems suggests that the Lorenz construction may represent a specific instance of a more general phenomenon. The systematic methodology developed here, comprising permutation-based enumeration with statistical characterization and topological precursor analysis, provides a template for such investigations.

ACKNOWLEDGMENTS

This research was conducted independently at the Departamento de Física, Universidad de Chile, without external funding.

DECLARATION OF GENERATIVE AI AND AI-ASSISTED TECHNOLOGIES IN THE WRITING PROCESS

During the preparation of this work, the author used an AI language model to improve the readability and internal consistency of the text, and for assistance with background research. After using this tool, the author reviewed and edited the content as needed and takes full responsibility for the content of the publication.

- ¹B. A. Toledo, History-dependent dynamical invariants in the Lorenz system, *Chaos Solitons Fractals* **202**, 117468 (2026).
- ²A. J. Chorin, A. P. Kast, and R. Kupferman, Optimal prediction and the Mori-Zwanzig representation of irreversible dynamics, *Proc. Natl. Acad. Sci. USA* **97**, 2968 (2000).
- ³R. Zwanzig, *Nonequilibrium Statistical Mechanics* (Oxford University Press, Oxford, 2001).
- ⁴P. J. Morrison, A paradigm for joined Hamiltonian and dissipative systems, *Physica D* **18**, 410 (1986).
- ⁵S. A. Hojman, A new conservation law constructed without using either Lagrangians or Hamiltonians, *J. Phys. A: Math. Gen.* **25**, L291 (1992).
- ⁶R. Gilmore, Topological analysis of chaotic dynamical systems, *Rev. Mod. Phys.* **70**, 1455 (1998).
- ⁷E. N. Lorenz, Deterministic nonperiodic flow, *J. Atmos. Sci.* **20**, 130 (1963).
- ⁸S. H. Strogatz, *Nonlinear Dynamics and Chaos*, 2nd ed. (Westview Press, Boulder, 2015).
- ⁹J.-P. Eckmann and D. Ruelle, Ergodic theory of chaos and strange attractors, *Rev. Mod. Phys.* **57**, 617 (1985).
- ¹⁰P. Cvitanović *et al.*, *Chaos: Classical and Quantum* (Niels Bohr Institute, Copenhagen, 2005).